

## Pressure-Induced Amorphization in Silicon Caused by the Impact of Electrosprayed Nanodroplets

Manuel Gamero-Castaño,<sup>1,\*</sup> Anna Torrents,<sup>1</sup> Lorenzo Valdevit,<sup>1</sup> and Jian-Guo Zheng<sup>2</sup>

<sup>1</sup>*Department of Mechanical and Aerospace Engineering, University of California, Irvine, California 92697, USA*

<sup>2</sup>*Materials Characterization Center, Calit2, University of California, Irvine, California 92697, USA*

(Received 8 June 2010; revised manuscript received 31 August 2010; published 28 September 2010)

This Letter describes the shock-induced amorphization of single-crystal Si bombarded by nanodroplets. At impact velocities of several kilometers per second, the projectiles trigger strong compression pulses lasting tens of picoseconds. The phase transition, confirmed via transmission electron microscopy and electron backscatter diffraction, takes place when the projectile's stagnation pressure is approximately 15 GPa. We speculate that the amorphization results either from the decompression of the  $\beta$ -Sn phase or during the compression of the diamond phase.

DOI: 10.1103/PhysRevLett.105.145701

PACS numbers: 64.70.K-, 62.50.Ef

Silicon exhibits several high-pressure phase transitions. In particular, the first transition encountered on increasing the pressure takes the standard cubic diamond configuration (Si-I) to a  $\beta$ -Sn metallic phase (Si-II) [1]. The transition takes place at 11.3 GPa under hydrostatic compression at room temperature [2] and at stresses between 10 and 12 GPa in uniaxial shock-wave experiments [3]. The reconstructive transition is irreversible at ambient temperature, yielding two metastable crystalline configurations upon slow decompression. In addition to these crystalline phase transitions, indentation experiments at ambient temperature have shown that amorphization may also occur during fast decompression of the Si-II phase [4]. This amorphous state has never been observed in shock-wave experiments, even though decompression transients are much faster than what is possible in indentation. In fact, Si-I is the only phase observed in recovered shocked substrates [5]. Furthermore, although high-pressure amorphization during compression has been documented in Si nanoparticles, it has never been observed in bulk Si. In the case of the nanoparticles, amorphization was prompted during quasistatic compression above 7–8 GPa [6].

Electrospraying in the cone-jet mode is an atomization technique suitable for producing beams of charged nanodroplets. In a vacuum, these projectiles can be electrostatically accelerated to velocities of several kilometers per second, and the resulting impacts on crystalline solids such as Si, SiC, and B<sub>4</sub>C produce sputtering yields in excess of one [7]. The drop diameter can be continuously varied from a few nanometers to tens of microns by adjusting the flow rate and the physical properties of the fluid [8]. Electrosprayed nanodroplets are then ideal to study size effects in the collision of an energetic projectile with a surface, in the unexplored range between atomic and cluster ions in one hand (particle sizes under a few nanometers), and the smallest macroscopic projectiles used in the field of hypervelocity impact. The amorphization presented in this Letter is an example of the new phenomena made possible by nanodroplet projectiles.

In the present work we electrospray inside a vacuum chamber the ionic liquid 1-ethyl-3-methylimidazolium bis(trifluoromethylsulfonyl) imide, C<sub>8</sub>H<sub>11</sub>F<sub>6</sub>N<sub>3</sub>O<sub>4</sub>S<sub>2</sub>, by using the experimental arrangement described in Ref. [9]. A fraction of the beam is accelerated towards a Si wafer, impacting at near normal angle with the (100) surface. The charge to mass ratio  $\xi$  of the drops is measured with a time-of-flight spectrometer; the impact velocity is computed with  $\xi$  and the acceleration voltage  $V_A$ ,  $v = \sqrt{2\xi V_A}$ ; the stagnation pressure of the projectile and the kinetic energy of its molecules are  $P = \rho v^2/2$  and  $E_m = m_m \xi V_A$ , respectively, where the liquid density and molecular mass are  $\rho = 1520 \text{ kg/m}^3$  and  $m_m = 391.31 \text{ amu}$ , respectively. The drops' charges and diameters exhibit relatively narrow distributions, the smallest drops having the highest charge to mass ratios and therefore the highest impact pressures [9]. The electrospray in this work has a total current of 297 nA; the current impinging on the wafer is 12 nA; and the average diameter and charge to mass ratio of the drops are 29 nm and 853 C/kg, respectively. The stagnation pressure and the molecular energy for the average drop and a typical 15 kV acceleration voltage are 19.4 GPa and 51.9 eV, respectively.

Figure 1 shows the damage caused by beamlets with acceleration voltages between 9.5 and 17.5 kV, after 15 minutes of bombardment. The central ovoid in each picture is the impact region, has a depth of several microns, and is surrounded by a deeper ditch and a thin film of sputtered deposits. Constructive interference of polychromatic light reflected from the surfaces of the thin film and the wafer, together with the varying film thickness, produces the iridescent rings. At acceleration voltages up to 11.0 kV, the ovoid is formed by a multitude of intertwined craters with diameters of the order of a micron and depths of a few hundred nanometers [9]. This rough surface is optically diffusive and therefore shines in the normal line of sight when illuminated at a glancing angle [see Figs. 1(a) and 1(b)]. At 12.5 kV [Fig. 1(c)], the topography of the

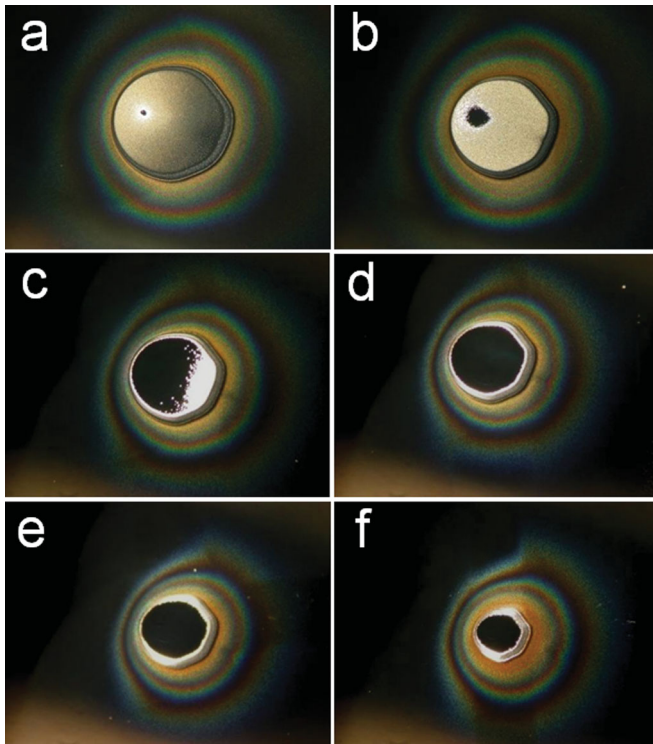


FIG. 1 (color). Si targets bombarded by a nanodroplet beamlet at acceleration voltages of (a) 9.5, (b) 11.0, (c) 12.5, (d) 14.0, (e) 15.5, and (f) 17.5 kV. The central ovoid is the impact region, while the surrounding iridescent rings are formed by a thin film of deposits.

impact region changes noticeably as most of the bright, cratered area is substituted by a smooth and specular surface. The rms of this surface can be as small as 2.9 nm [7]. At still higher acceleration voltages, the micron-sized craters completely disappear, and the beamlet carves only the specular surface and the surrounding ditch. The sputtering yield also changes significantly when the carved surface becomes specular: Before this point it increases with acceleration voltage, but at higher energies it first decreases and then remains approximately constant [9]. It is worth noting that at 11.0 and 12.5 kV the stagnation pressures are 14.3 and 16.2 GPa, respectively, which are near the transition pressure between the Si-I and Si-II phases.

The discontinuity in the surface topology and the sputtering yield hints at a profound change in the microstructure of the target. This is confirmed by the electron backscatter diffraction (EBSD) maps of Fig. 2. The measurements were performed with a Zeiss UltraPlus scanning electron microscope (SEM) equipped with an Oxford EBSD detector and HKL CHANNEL5 FLAMENCO software. The SEM was operated at 15 kV. Figure 2(a) examines the impact region in Fig. 1(f). The SEM image shows the specular area surrounded by the ditch and a small fraction of the deposits. The inset to the right is a crystal orientation map (color scale) superimposed on a gray background indicative of the surface's shape. Only the points with the

cubic diamond structure are assigned a color, which is allocated according to the crystallographic direction along the surface's normal. For example, red marking indicates that the point is Si-I with the [100] direction along the normal. The cubic diamond phase is indexed throughout the ditch, while very few cubic diamond points are indexed in the specular surface. In fact, the diffraction patterns in the specular surface display either diffusive scattering without any Kikuchi bands or very weak bands, and therefore this gray area is amorphous. The deposited film is also amorphous, probably because the sputtered Si and the projectile material form a new compound. This is suggested by energy-dispersive x-ray spectrometry, which detects Si as the only element present in the impact region, and a combination of Si, C, N, O, F, and S in the deposition area. To ensure that the crystal mapping is not an artifact of the geometry or defocusing of the electron beam over a wide area, we extended the analyzed region to include as a reference the single crystal free of deposits, as shown in the bottom-left inset. This image confirms that the ditch is mostly crystalline and that the specular surface is amorphous. Finally, Fig. 2(b) shows the crystal orientation map of an area with cratered and specular surfaces, i.e., a sample similar to Fig. 1(c) carved at a transitional beam energy. The presence of both types of surfaces is likely due to the spread in the projectiles' velocities and the angular separation of the projectile velocities induced by the space charge of the beamlet. There is a clear difference in the crystallinity of both surfaces: The specular area is mostly amorphous, while the area with micron-sized craters remains largely crystalline, with the same orientation as the pristine Si wafer. In summary, the EBSD data collectively show that the specular surfaces carved by the more energetic beams are amorphous, while the micron-sized craters produced at lower energies remain crystalline.

We have also characterized the microstructural changes of the crystalline target via transmission electron microscopy (TEM). To protect the as-bombarded surface, a 40 nm carbon layer was deposited on it. A FEI Helios focused-ion-beam machine was used to carefully cut cross-sectional specimens. Energy-filtered TEM images were digitally recorded in FEI Titan and TF20 machines equipped with a Gatan energy filter, and high-resolution TEM images were recorded in FEI Titan and TF30UT machines. To ensure that the Si (100) surfaces were edge-on, the specimens were tilted to the  $[01\bar{1}]$  zone axis, which is perpendicular to the cross section. Figure 3(a) is a bright field TEM micrograph of the cross-sectional specimen showing the crystalline substrate, an amorphous Si layer, and the amorphous carbon layer used for protection. The amorphous Si layer is about 30 nm thick and exhibits several brighter patches, possibly indicative of lower density areas. The dotted line approximately marks the position of the top surface of the amorphous Si layer. The interface between the amorphous Si and carbon layers

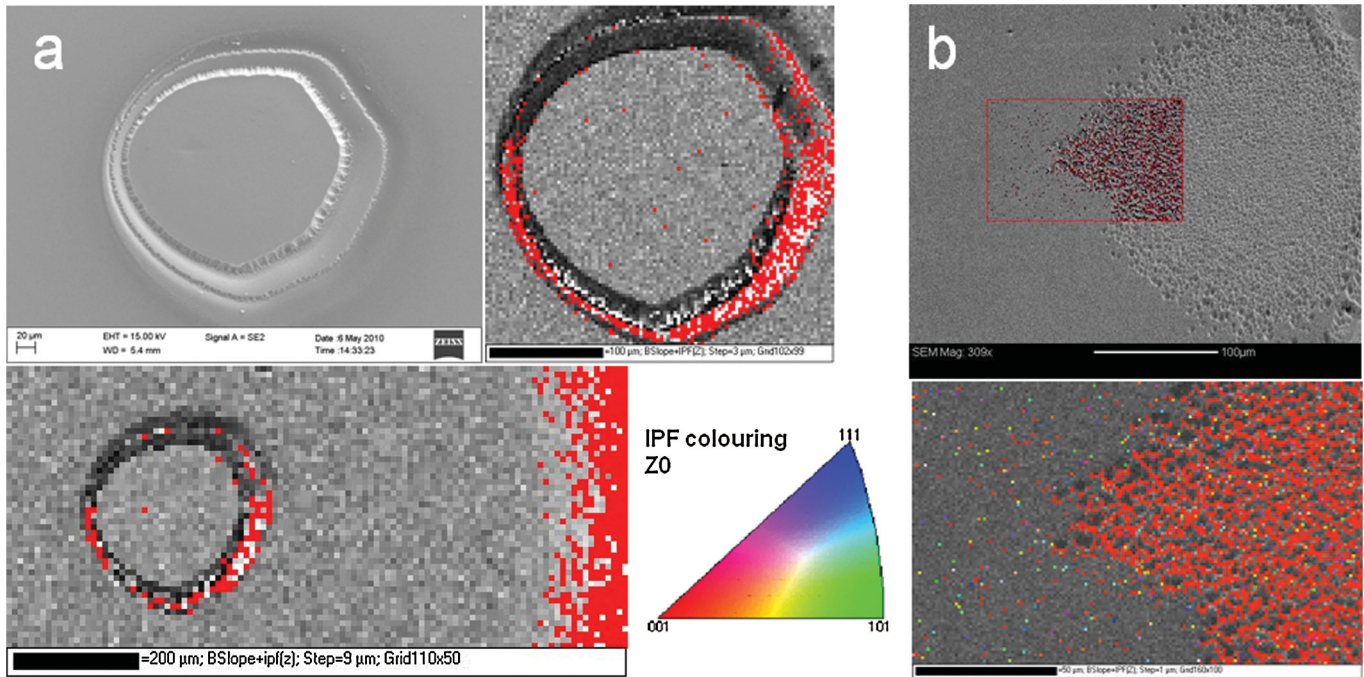


FIG. 2 (color). (a) SEM image (top left) and EBSD crystal orientation map (top right) of the specular surface and surrounding ditch in Fig. 1(f). Only Si-I points are assigned a color (see the inverse pole figure scale), where red implies that the crystal's [100] direction is along the surface's normal. Gray areas are indicative of amorphous material. Bottom left: The EBSD map includes the deposition area (an amorphous mixture of Si, C, N, O, F, and S) and the original Si-I surface on the far right. (b) SEM image (top) and EBSD map (bottom) of a bombarded area with cratered and specular surfaces. The specular region is amorphous Si, while the micron-sized craters are mostly crystalline.

can be resolved with the energy-filtered TEM [Figs. 3(b) and 3(c)], which were recorded with Si  $L$ -edge and C  $K$ -edge energy-loss electrons, yielding silicon and carbon maps, respectively. Finally, a detail of the amorphous and crystalline Si interface is shown in Fig. 3(d) as a HRTEM image: The Si lattice is easily seen as the crystalline area in the lower section, while the amorphous phase is the disordered arrangement on top of it. The insets in Fig. 3(d) are the fast Fourier transform of the crystalline and amorphous phases: The bright spots are readily indexed as lattice planes of the cubic diamond structure in the  $[01\bar{1}]$  zone axis, while the isotropy of the amorphous phase is patent in the upper inset.

The disappearance of the crystalline order is an example of pressure-induced amorphization [10], resulting from the hypervelocity impact of nanodrops and the associated shock compression [11]. Despite their small size, the drops are significantly larger than the target's mean free path for atomic collisions (of the order of the average distance between neighboring atoms, 0.27 nm for Si-I), and therefore the substrate responds to the impact as a continuum. This has been demonstrated by Samela and Nordlund, whose molecular dynamics simulations show how the impact of Au clusters as small as 3.3 nm already exhibit the continuum characteristics of much larger macroprojectiles [12]. In this continuum scenario, impacts at the velocities studied in this Letter produce shock waves that

penetrate through the target, leaving behind a highly pressurized material. In particular, in the vicinity of the point of impact the target is pressurized near the stagnation pressure of the drop. The impact also triggers a second shock wave in the drop, moving in the opposite direction. Upon arrival to the drop's free surface, the shock unloads into the vacuum and triggers a rarefaction wave that moves towards the target decompressing and vaporizing the liquid. The rarefaction wave continues through the target, unloading the compressed silicon [13]. A rough but sufficient estimate for the time lag between the shock and unloading waves is the ratio between the droplet's velocity and its diameter. For example, at the transition acceleration voltage of 12.5 kV the impact velocity of the 29 nm droplets is 4620 m/s, and the lag time is of the order of 6 ps.

The response of crystalline solids to various loading paths is not yet well understood. For example, in the case of bulk Si, amorphization is known to take place during decompression of the Si-II phase in indentation research at room temperature [4], while it does not occur during decompression of the Si-II phase in macroscopic shock experiments [5]. We think that the amorphization described in this Letter, a novelty for shock-compressed Si, is due to the much smaller size of our projectiles and possibly to the associated brief compression which is known to affect the response of Si. For example, Loveridge-Smith *et al.* have shown that, during uniaxial shock compression

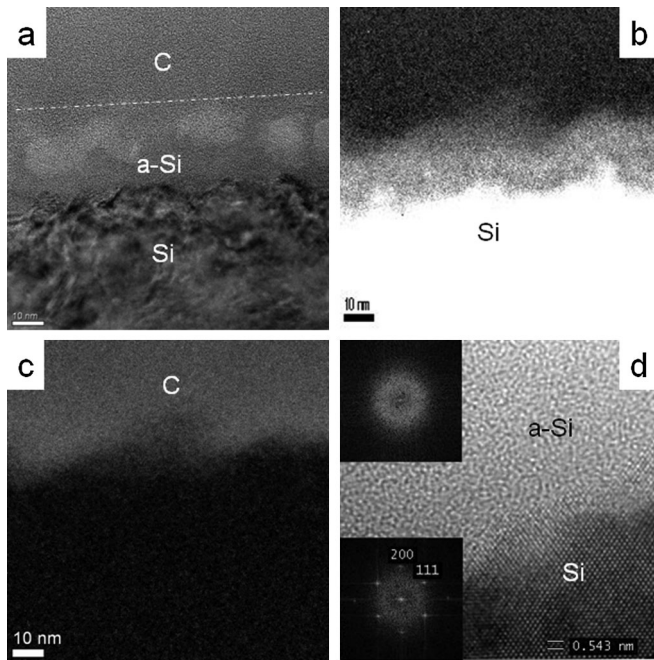


FIG. 3. TEM images of a sample from the specular surface in Fig. 1(e). The nanodrops amorphize a surface layer with a depth of approximately 30 nm, visible between a protective C layer and the crystalline Si substrate. (a) Bright field TEM micrograph of the cross section displaying the C layer, amorphous Si layer, and crystalline Si substrate; (b) Si map recorded with Si  $L$ -loss electrons; (c) C map imaged with C  $K$ -loss electrons; (d) high-resolution TEM image of the interface between crystalline and amorphous Si. The top inset is the fast Fourier transform pattern of the amorphous area, and the bottom inset is the fast Fourier transform pattern of crystalline Si.

lasting a few nanoseconds, single-crystal Si remains elastic well beyond the elastic limit associated with static compression. This behavior was attributed to the brief extent of the compression, which is much smaller than the characteristic time associated with the motion of the dislocations needed for plastic flow [14]. This observation has been ratified by Kalantar *et al.* in similar uniaxial experiments [15]. Kalantar *et al.* also make a statement most relevant to our study, namely, that the time scale for the Si-I  $\rightarrow$  Si-II transition is larger than a few nanoseconds, the typical compression time in their work.

We can think of two mechanisms explaining the observed amorphization. In the first one, Si undergoes the familiar Si-I  $\rightarrow$  Si-II transition under compression, followed by the Si-II  $\rightarrow$   $a$ -Si amorphization characteristic of indentation experiments at room temperature. The amorphous phase does not remain in macroscopic shock-recovered substrates, probably because, being heated by the compression, it can overcome the energy barrier separating it from the energetically favored Si-I phase [10]. Conversely, the small region surrounding the nanodroplet impact cools down very fast by heat conduction, and the decompression essentially occurs under cold conditions

like in indentation experiments. In the second mechanism, the Si-I  $\rightarrow$  Si-II transition is kinetically prevented, and the amorphization progresses directly from the Si-I phase during compression: The reconstructive nature of the Si-I  $\rightarrow$  Si-II transformation involves substantial long-range diffusion from nucleation sites; however, diffusion is hindered by high pressures, and the characteristic time for the completion of the transition may far exceed the compression pulse. If the statement by Kalantar *et al.* regarding the sluggish kinetics of the Si-I  $\rightarrow$  Si-II transition is valid, the Si-II phase will never form in a nanodroplet impact. It would then be reasonable to expect that, as the Si-I phase is compressed beyond its thermodynamic stability domain, the lattice will progressively deform without being able to transform to Si-II and will eventually lose its long-range order, becoming amorphous.

As a continuation to this research we plan to examine the occurrence of shock-induced amorphization in other materials (quantifying it in terms of the amplitude and width of the pressure pulse, and substrate's temperature) and investigate the use of nanodroplet beams for patterning amorphous layers on crystalline surfaces.

The authors thank Dr. S. J. Xue and Mr. B. Myers for their assistance in focused-ion-beam specimen preparation and TEM characterization. The authors acknowledge the Carl Zeiss Center for Excellence in Electron Microscopy at the University of California, Irvine. This work was partially supported by DARPA Young Faculty Grant No. N66001-10-1-4039.

\*Corresponding author.

mgameroc@uci.edu

- [1] A. Mújica *et al.*, *Rev. Mod. Phys.* **75**, 863 (2003).
- [2] J. Z. Hu *et al.*, *Phys. Rev. B* **34**, 4679 (1986).
- [3] S. D. Gilev and A. M. Trubachev, *J. Phys. Condens. Matter* **16**, 8139 (2004).
- [4] D. R. Clarke *et al.*, *Phys. Rev. Lett.* **60**, 2156 (1988).
- [5] H. Kishimura and H. Matsumoto, *J. Appl. Phys.* **103**, 023505 (2008).
- [6] S. K. Deb *et al.*, *Nature (London)* **414**, 528 (2001).
- [7] M. Gamero-Castaño and M. Mahadevan, *J. Appl. Phys.* **106**, 054305 (2009).
- [8] J. Fernández de la Mora, *Annu. Rev. Fluid Mech.* **39**, 217 (2007).
- [9] M. Gamero-Castaño and M. Mahadevan, *Appl. Surf. Sci.* **255**, 8556 (2009).
- [10] S. M. Sharma and S. K. Sikka, *Prog. Mater. Sci.* **40**, 1 (1996).
- [11] G. E. Duvall and R. A. Graham, *Rev. Mod. Phys.* **49**, 523 (1977).
- [12] J. Samela and K. Nordlund, *Phys. Rev. Lett.* **101**, 027601 (2008).
- [13] Y. B. Zel'dovich and Y. P. Raizer, *Physics of Shock Waves and High-Temperature Hydrodynamic Phenomena* (Dover, Mineola, 2002).
- [14] A. Loveridge-Smith *et al.*, *Phys. Rev. Lett.* **86**, 2349 (2001).
- [15] D. H. Kalantar *et al.*, *Phys. Plasmas* **10**, 1569 (2003).